# Using one-step facile and solvent-free mechanochemical process to synthesize photoactive $Fe_2O_3$-$TiO_2$ in treatment of industrial wastewater

Wennie Subramonian, Ta Yeong Wu* and Siang-Piao Chai

Chemical Engineering Discipline, School of Engineering, Monash University, Jalan Lagoon Selatan, 47500 Bandar Sunway, Selangor Darul Ehsan, Malaysia.

*Corresponding author: Ta Yeong Wu

**E-mail addresses**: wu.ta.yeong@monash.edu; tayeong@hotmail.com

**Tel.**: +60 3 55146258

**Fax**: +60 3 55146207

## ABSTRACT

In this present study, $Fe_2O_3$-$TiO_2$ photocatalyst was synthesized and used to degrade real industrial wastewater, namely pulp and paper mill effluent (PPME). $Fe_2O_3$-$TiO_2$ was synthesized via ball milling at ambient conditions without incorporating any solvent. Comprehensive characterization studies and photocatalytic evaluations of the synthesized $Fe_2O_3$-$TiO_2$ were conducted in this study. It was verified that $Fe_2O_3$-$TiO_2$ possessed crystalline structures of γ-$Fe_2O_3$, anatase and rutile $TiO_2$. Also, a good dispersion of Fe and O elements within the $TiO_2$ framework could be attained. A detection of Fe-O-Ti bond elucidated a substitution of $Ti^{4+}$ by $Fe^{3+}$ in the $TiO_2$ lattice sites through mechanical milling, which ultimately enhanced the

photocatalytic activities of $Fe_2O_3$-$TiO_2$. Moreover, $Fe_2O_3$-$TiO_2$ exhibited enhanced catalytic properties in terms of specific surface area (58.40 $m^2/g$), porosity (0.29 $cm^3/g$), band gap (2.95 eV), and charge separation in comparison with commercial P25. The present work also proved that both characteristics and photoactivity of $Fe_2O_3$-$TiO_2$ were significantly affected by its synthesis conditions (milling time, milling speed, and $Fe_2O_3$ loading). The highest treatment efficiency of PPME (62.3% of chemical oxygen demand or COD removal) was achieved using $Fe_2O_3$-$TiO_2$, which was synthesized at 20 min, 250 rpm and 1 mol% of milling time, milling speed and $Fe_2O_3$ loading, respectively. Noticeably, the photoactivity of the $Fe_2O_3$-$TiO_2$ was more superior than the P25 (40.6% of COD removal). This study proved that mechanochemical process enabled the green synthesis of $Fe_2O_3$-$TiO_2$ that could be used in treatment of real industrial wastewater.

***Keywords:*** Ball milling; Iron (III) oxide; Titanium (IV) oxide; Photocatalysis; Pulp and paper mill effluent; Wastewater treatment

## 1. Introduction

Pulp and paper mills are one of the major sources of industrial pollution worldwide, in which pulp and paper effluent (PPME) contains high amount of total suspended solids, chemical oxygen demand (COD), and other toxic contaminants [1]. However, most PPME treatment plants apply biological treatment systems, which result in ineffective removal of colour and toxicity from the effluent [2]. As an alternative, advanced oxidation processes (AOPs) have been proposed in wastewater treatment systems to effectively oxidize recalcitrant pollutants into biodegradable intermediates and innocuous compounds (i.e. carbon dioxide and water) due to the generation of highly potent oxidant, hydroxyl radicals (·OH) [3,4]. Other advantages of AOPs include colour removal from the wastewater, lower sludge production, and simplicity in operation [5]. Among several AOPs, powerful oxidants such as ozone, hydrogen peroxide, and potassium permanganate have been studied in photocatalysis of wastewater. Typically, these oxidants were used in homogenous photocatalysis processes, which incurred instability and difficulty in catalyst separation process [6]. Conversely, heterogeneous photocatalysis is deemed as the most economically profitable and environmentally safe technology among other AOPs in the removal of organic pollutants from water systems [7]. Hence, heterogeneous photocatalysis was employed as a promising treatment route to degrade highly contaminated PPME in this current study.

Numerous studies have established that $TiO_2$ as one of the most promising photocatalysts to initiate photocatalytic reactions, owing to its optical and electronic properties, strong oxidizing power, chemical inertness, high stability, non-toxicity, corrosion resistant, inexpensiveness, and environmentally benign nature as compared to other photocatalysts [8-10]. However, $TiO_2$ has a

wide band gap (anatase phase: 3.2 eV and rutile phase: 3.0 eV) and presents a high recombination rate of photogenerated electron-hole pairs [11,12]. In view of this, coupling of $TiO_2$ with other metal oxides (e.g. $Fe_2O_3$ [13], $WO_3$ [14], ZnO [15], $SnO_2$ [16], and $CeO_2$ [17]) was investigated extensively for its potential application in degradation of organic pollutants. Generally, the synthesis of these hybrid metal oxides photocatalysts employed conventional methods (such as sol-gel, hydrothermal, solvothermal, precipitation, and chemical/physical vapour deposition) that posed several drawbacks. These conventional methods were predominantly multi-step procedures, necessitated the utilization of toxic metal-organic precursors, and required expensive equipment [18,19]. Also, longer duration was needed, which was undesirable for industrial fabrication purposes [18]. Therefore, development of a greener and facile fabrication method using non-solvent synthesis under ambient temperature and atmospheric pressure was pursued in the current work.

Green chemistry was an initiative driven by the U.S. Environmental Protection Agency in the early 1990. It involved the design of chemical products and processes that reduced or eliminated the need and generation of hazardous substances [20]. Growing emphasis on green chemistry led to the use of mechanochemical process as a prospective method to activate and fabricate a photocatalyst under a solvent-free condition [21]. Previously, mechanochemical reaction was applied widely in areas including material synthesis, coal industry, extractive metallurgy, powder surface modification, pharmacy, and waste management [22]. During the course of mechanochemical process via ball milling (mechanical milling), accumulated potential energy with shear and friction forces were transferred from milling balls to the materials. This energy induced severe plastic deformation as well as created new interfaces and defects on the materials, which potentially led to substantial improvement in material properties of the final

product [23-25]. Mechanochemical process has gained importance over conventional synthesis methods because of its greener and facile technique [8,18]. In comparison with conventional synthesis methods, mechanochemical process did not require solvents and thus, no wastes were generated from catalyst washing. It also eliminated the need of multi-step procedures, high temperature and pressure conditions, plus no additions of hazardous and expensive chemicals were required [25,26]. Moreover, mechanochemical process yielded large quantities of desired product at ambient conditions within a very short processing time [8,18]. The advantages from this process serve as a very lucrative aspect from an economical viewpoint, thus, making mechanochemical synthesis very attractive for large-scale industrial production [18].

Herein, the current study demonstrated a facile and solvent-free mechanochemical process via mechanical milling to synthesize $Fe_2O_3$-$TiO_2$ photocatalyst as an approach towards a greener process. The synthesized $Fe_2O_3$-$TiO_2$ was used in degrading real PPME. To the best of our knowledge, there has been no report concerning the use of mechanochemically fabricated $Fe_2O_3$-$TiO_2$ photocatalyst in treating real industrial effluent, such as PPME. Thus, a detailed characterization study was performed to closely examine the structural and textural properties of the fabricated $Fe_2O_3$-$TiO_2$ via mechanochemical process. To further understand mechanochemical process, effects of fundamental synthesis conditions (i.e. milling time, milling speed, and $Fe_2O_3$ loading) on the properties and photoactivity of $Fe_2O_3$-$TiO_2$ were studied.

## 2. Experimental details

### 2.1. Materials

Iron (III) oxide, tungsten (VI) oxide, zinc oxide, cerium (IV) oxide, anatase titanium (IV) oxide, rutile titanium (IV) oxide, and Aeroxide® P25 were purchased from Sigma-Aldrich. All chemicals were used as received without further modification. Raw PPME was collected from Muda Paper Mills Sdn. Bhd., Kajang, Selangor. According to Subramonian et al. [27], raw PPME should be pre-treated using coagulation process to reduce the amount of total suspended solids from the effluent. In this study, PPME was pre-treated to the methods proposed by Subramonian et al. [28] and the pre-treated PPME with lesser suspended solids was used to evaluate the photocatalytic performance of the synthesized $Fe_2O_3$-$TiO_2$.

### 2.2. Mechanochemical synthesis of $Fe_2O_3$-$TiO_2$

$Fe_2O_3$-$TiO_2$ photocatalyst was fabricated in the absence of solvent via mechanochemical process using a planetary ball mill (Fritsch Pulverisette 5). Two zirconia vials with 500 $cm^3$ capacity were filled with a stoichiometric amount of $Fe_2O_3$ and P25 powder. 10 mm diameter balls were used as milling medium. Ball to powder mass ratio was kept constant at 10:1. Effect of mechanochemical synthesis conditions on the fabricated photocatalyst was studied by varying the milling time (10-30 min), milling speed (150-350 rpm), and $Fe_2O_3$ molar content (0.4-1.2 mol%). The synthesized $Fe_2O_3$-$TiO_2$ was then characterized and its catalytic performance was evaluated based on COD removal of PPME.

130 **2.3. Characterization study**

131 Crystallinity and phase identification of samples were determined from powder X-ray
132 diffraction (XRD) patterns. XRD data was recorded on a X-ray diffractometer (Bruker D8
133 Discovery) using Ni filtered Cu-Kα radiation (λ = 0.154056 nm) at a scan rate of 0.02° $s^{-1}$. The
134 accelerating voltage and current were 40 kV and 40 mA, respectively. Crystallite sizes of the
135 samples were calculated based on Scherrer formula. Surface morphology and elemental
136 compositions of the samples were obtained using field electron scanning electron spectroscopy
137 (FESEM) (Hitachi SU8010) equipped with energy-dispersive X-ray (EDX). X-ray photoelectron
138 spectroscopy (XPS) analysis was conducted on a Kratos Axis-Ultra DLD instrument with a
139 monochromatized Al Kα X-ray source (15 kV, 200 W) at a pressure of $7.6 \times 10^{-9}$ Torr and 20 eV
140 pass energy. All binding energies were referenced to C 1s peak at 284.6 eV of the adventitious
141 carbon. Transmission electron microscopy (TEM) images were taken with a JEOL JEM-2100F
142 microscope operated at 200 kV. Meanwhile, textural properties of the samples were analyzed
143 based on nitrogen adsorption/desorption isotherms using Micromeritics, ASAP 2020. Specific
144 surface areas and pore distributions were determined from Brunauer-Emmett-Teller (BET) and
145 Barrett-Joyner-Halenda (BJH) methods, respectively. Raman spectra were acquired using
146 HORIBA Scientific, LabRAM HR Evolution with an excitation wavelength of 514 nm under
147 room temperature whereas Fourier transform infrared (FTIR) spectra were recorded over a range
148 of 4000-400 $cm^{-1}$ at room temperature using a FTIR spectrophotometer (Thermo Scientific
149 Nicolet iS10). Additionally, ultraviolet-visible (UV-vis) diffused reflectance spectra (DRS) were
150 recorded on a UV-vis spectroscopy (Cary 100, Agilent) with $BaSO_4$ as reference. Band gap
151 energies of the samples were estimated from plot of transformed Kubelka-Munk function $[F(R) \cdot h\nu]^{1/2}$ against abscissa of photon energy ($h\nu$). Photoluminescence (PL) emission spectra was

analyzed using a fluorescence spectrometer (LS55, Perkin Elmer) at an excitation wavelength of 315 nm with 500 nm $min^{-1}$ scanning speed. The widths of the excitation and emission slits were fixed at 10 nm.

### 2.4. Photocatalytic evaluation of $Fe_2O_3$-$TiO_2$

Photoactivity of the prepared $Fe_2O_3$-$TiO_2$ was evaluated in terms of photodegradation of PPME. In a typical procedure, 1.0 g/L of $Fe_2O_3$-$TiO_2$ was dispersed in 50 mL of PPME at pH 4. The suspension was magnetically stirred in the dark at 800 rpm for 30 min to achieve adsorption-desorption equilibrium. Then, the suspension was exposed to UV irradiation (400 W of UV lamp) for 3 h under continuous stirring and aeration (air flow rate = 4.0 L/min). The initial and final samples were withdrawn from the suspension before and after irradiation to determine a change in COD (Equation (1)). Photocatalyst was removed from the samples by centrifugation (13500 rpm for 15 min).

$$COD\ removal, \% = \frac{COD_{initial} - COD_{final}}{COD_{initial}} \times 100 \qquad (1)$$

## 3. Results and discussion

### 3.1. Effect of mechanical milling on characteristics and photoactivity of $Fe_2O_3$-$TiO_2$

In mechanochemical synthesis, metal oxide powders ($Fe_2O_3$ and $TiO_2$) were plastically deformed due to high-energy impact between milling balls and wall of the vial, producing the final composite $Fe_2O_3$-$TiO_2$ [8]. Fundamental mechanochemical synthesis conditions played a crucial role in manipulating photocatalytic properties of $Fe_2O_3$-$TiO_2$ [7]. Therefore, the present

176 study investigated the effect of mechanochemical process conditions (milling time, milling
177 speed, and loading of $Fe_2O_3$) on the intrinsic properties and photoactivity of $Fe_2O_3$-$TiO_2$.
178
179 **3.1.1. Effect of milling time**
180 Change in $Fe_2O_3$-$TiO_2$ morphology as a function of milling time was observed from FESEM
181 images. Mechanically milled $Fe_2O_3$-$TiO_2$ samples were gradually ground to finer particles from
182 10 to 20 min (Fig. 1a-c) due to longer duration of impact and shear forces incurred from the
183 milling balls. However, prolonging the milling time above 20 min resulted in highly
184 agglomerated particles with rough surfaces (Fig. 1d and e). Similar findings were observed by
185 House et al. [29]. Powder that was milled at 25 and 30 min had a high surface energy, which
186 facilitated the powder to reunite and reagglomerate in order to reduce surface energy and re-
187 stabilize the system [30]. In short, fracture of solids only occurred at shorter milling time
188 whereas reagglomeration appeared at longer milling time [31]. Surface morphology of $Fe_2O_3$-
189 $TiO_2$, P25 and $Fe_2O_3$ powder were also compared. From the FESEM images, P25 powder (Fig.
190 1f) consisted of uniform spherical particles whereas $Fe_2O_3$ (Fig. 1g) particles were large and
191 irregular-sized. The fabricated $Fe_2O_3$-$TiO_2$ (Fig. 1a-c) photocatalyst was finer than $Fe_2O_3$ (Fig.
192 1g). In addition, $Fe_2O_3$-$TiO_2$ (Fig. 1a-c) was irregular in shape, randomly organized, and slightly
193 agglomerated as compared to P25 (Fig. 1f). Carneiro et al. [8] also reported very similar catalyst
194 morphology that was induced by the effect of ball milling.
195 An employment of mechanochemical synthesis was reported to promote mesoporosity and
196 change in specific surface area of the materials [32]. Hence, surface properties of the synthesized
197 $Fe_2O_3$-$TiO_2$ were evaluated at different milling time and were compared with $Fe_2O_3$ and pristine
198 P25. According to IUPAC classification, nitrogen adsorption/desorption isotherm of $Fe_2O_3$-$TiO_2$

showed a typical type IV pattern with a hysteresis loop beginning around relative pressure of 0.7 (Fig. 2). The pattern suggested the occurrence of mesoporous structure with a broad pore size distribution [32,33]. Pore size distribution curve (inset in Fig. 2) depicts a wide range of pore diameter from 4 to 35 nm with the pore size mainly distributed at 17 nm, implying that an incorporation of $Fe_2O_3$ into $TiO_2$ lattice through mechanochemical synthesis did not defect the surface mesoporous structure of the $TiO_2$ [34]. Specific surface area, pore volume, and pore size of $Fe_2O_3$-$TiO_2$ were found to be higher than P25 (Table 1). Higher textural properties provided better surface adsorption and mass transfer between organic pollutants and $Fe_2O_3$-$TiO_2$ in the catalyst pore, suggesting a potential enhancement in photocatalytic activity [34].

The specific surface areas, pore volumes, and pore sizes of the milled samples were also clearly affected by the milling time (Table 2). Overall, the aforementioned textural properties improved from milling time 10 to 20 min because of repeated fracturing of solids induced by the milling balls, which consequently led to a reduction in particle size, and an increase in both surface area and porosity [31]. However, a deterioration of textural properties occurred from 25 to 30 min due to reagglomeration of solids as evidenced in Fig. 1d and e. Similarly, the photocatalytic trend also displayed a gradual increase in COD removal (52.7 to 62.3%) from 10 to 20 min, followed by a decrease (57.4 to 52.8%) from 25 to 30 min of milling time (Fig. 3). One-way analysis of variance (ANOVA) revealed that the recommended milling time was 20 min. Thus, subsequent synthesis of $Fe_2O_3$-$TiO_2$ photocatalyst was carried out based on this milling time.

### 3.1.2. Effect of milling speed

Change in milling speed stimulated modifications to the crystallite structure of $Fe_2O_3$-$TiO_2$. It was proven in this study that by increasing the milling speed (150 to 350 rpm), XRD diffraction peaks (Fig. 4) became broader with diminishing intensities. The result denoted the presence of smaller-sized particles formed at elevated milling speed [8]. Besides, crystallite sizes of $Fe_2O_3$-$TiO_2$ also decreased with increasing milling speed (150 to 350 rpm) as shown in Table 3. Mechanical impact from the milling balls at rising milling speed deformed the powders and introduced lattice defects, leading to a reduction in crystallite size [8]. Fig. 5 shows an improvement in catalytic activity from 150 to 250 rpm (52.2 to 62.3% of COD removal, respectively) followed by a drop from 300 to 350 rpm (53.2 to 50.2% of COD removal, respectively). Decline in photoactivity at elevated milling speed was attributed to higher rutile content in $Fe_2O_3$-$TiO_2$ at 300 to 350 rpm (Table 3). The rutile phase fraction for each sample (Table 3) was determined from the XRD patterns (Fig. 4) using Spurr equation. At higher milling speed, more collisions occurred between the milling balls and powders. Following that, an increase of local temperature and pressure at the collision sites induced an anatase-to-rutile phase transformation of the fabricated $Fe_2O_3$-$TiO_2$ [8]. One-way ANOVA suggested that 250 rpm was the recommended milling speed to prepare $Fe_2O_3$-$TiO_2$ and subsequent milling was carried out using this speed.

In addition, XRD patterns of the synthesized $Fe_2O_3$-$TiO_2$ (Fig. 4) exhibited characteristic peaks of $Fe_2O_3$, anatase, and rutile $TiO_2$. Peaks at 25.3, 37.8, 48.1, 54.4, 55.1, 62.7, 69.0, and 75.1°corresponded to (101), (004), (200), (105), (211), (204), (116), and (215) planes, respectively of anatase $TiO_2$ (JCPDS card file: 21-1272). Trace amounts of rutile $TiO_2$ present in $Fe_2O_3$-$TiO_2$ were represented at 27.4 , 36.0 , 39.2 , 54.2 , 56.7 , 69.9°, which were assigned to (110), (101), (200), (211), (220), and (112) planes, respectively (JCPDS card file: 21-1276). The

presence of both anatase and rutile phases was due to the mix phases of P25 (anatase: ~80% and rutile: ~20%) used as a material to fabricate $Fe_2O_3$-$TiO_2$. Meanwhile, traces of $Fe_2O_3$ present in $Fe_2O_3$-$TiO_2$ showed lower peak intensities at 30.2, 35.5, 57.0, and 62.9°, which were indexed to (220), (311), (511), and (440) planes, respectively (JCPDS card file: 39-1346). The low peak intensities were due to low concentration of $Fe_2O_3$ (1 mol%) added during the fabrication of $Fe_2O_3$-$TiO_2$ [12]. Upon closer observation, angular positions of certain XRD peaks of the synthesized $Fe_2O_3$-$TiO_2$ were slightly shifted as compared to the peaks of P25. This implied a small distortion in $TiO_2$ crystal lattice due to presence of Fe. The $TiO_2$ lattice distortion was a result from $Ti^{4+}$ replaced by $Fe^{3+}$ because of their comparable radii (0.068 and 0.064 nm, respectively) [8,35]. A substitution of $Ti^{4+}$ by $Fe^{3+}$increased the number of oxygen vacancies, which promoted photoactivity of $Fe_2O_3$-$TiO_2$ [35]. Overall, the XRD patterns of $Fe_2O_3$-$TiO_2$ established the coexistence of $Fe_2O_3$, anatase and rutile $TiO_2$ crystalline structures. Additionally, average crystallite sizes of $Fe_2O_3$-$TiO_2$, P25, and $Fe_2O_3$ were 22.99, 24.29, and 17.45 nm, respectively (Table 1).

### 3.1.3. Effect of $Fe_2O_3$ loading

PL measurement was conducted to evaluate the correlation between photoactivity of $Fe_2O_3$-$TiO_2$ and $Fe_2O_3$ loading. Peak intensity of PL spectra correlated to the recombination rate of electron-hole pairs whereby weaker peak intensity represented lower recombination rate [36]. According to the PL signals (Fig. 6), an addition of $Fe_2O_3$ from 0.4 to 1.2 mol% reduced the PL peak intensities, signifying better charge separation at higher $Fe_2O_3$ molar content. Due to the close radii of $Fe^{3+}$ (0.064 nm) and $Ti^{4+}$ (0.068 nm), an increase of $Fe_2O_3$ loading led to more substitution of $Ti^{4+}$ by $Fe^{3+}$, consequently, generating more oxygen vacancies [35]. An increase

267 in oxygen vacancies, which acted as electron donors in $TiO_2$ lattice, promoted better charge
268 separation. On the other hand, excessive addition of $Fe_2O_3$ could cause an undesirable energy
269 transfer between nearby ions due to shorter distance of Fe-Fe ions, leading to a deterioration in
270 charge separation and reduction in photoactivity [35]. As a comparison, the synthesized $Fe_2O_3$-
271 $TiO_2$ exhibited a significant 84% reduction in PL emission intensity as compared to P25 (Fig. 6).
272 The reduction of emission intensity signified a high efficiency of charge separation and transfer
273 between the two $Fe_2O_3$ and $TiO_2$ metal oxides in the synthesized $Fe_2O_3$-$TiO_2$ [37]. Theoretically,
274 an incorporation of $Fe_2O_3$ into $TiO_2$ lattice resulted in the substitution of $Ti^{4+}$ by $Fe^{3+}$ species,
275 creating oxygen vacancies, which in turn supported charge separation [35].

276 Band gap measurements from diffuse reflectance study pave way to a better understanding
277 of the optical response of fabricated $Fe_2O_3$-$TiO_2$ [38]. Band gaps of $Fe_2O_3$-$TiO_2$ samples at
278 different $Fe_2O_3$ loading are displayed in the transformed Kulbeka-Munk function plot (Fig. 7a).
279 Although the band gap values were in close range (2.85-2.95 eV) despite a change in $Fe_2O_3$
280 molar content, the photodegradation efficiency (Fig. 8) improved significantly from 40.6 to
281 62.5% with increasing $Fe_2O_3$ loading (0.4 to 1.2 mol%, respectively). Upon light absorption,
282 excited electrons from $TiO_2$ conduction band were transferred to the interface of $Fe_2O_3$ and
283 converted $Fe^{3+}$ into $Fe^{2+}$ [37,39]. Since the unstable $Fe^{2+}$ was rapidly oxidized by dissolved
284 oxygen to $Fe^{3+}$, $Fe^{3+}$ once again behaved as a shallow trapping site for photoexcited electrons
285 from $TiO_2$, hindering electron-hole pair recombination [36,39]. So, at higher $Fe_2O_3$ molar
286 content, more $Fe^{3+}$ was incorporated into $TiO_2$ lattice [40]. Thus, electron-hole recombination
287 was suppressed more effectively and enhanced the photoactivity of $Fe_2O_3$-$TiO_2$ [40]. However,
288 further addition of $Fe_2O_3$ beyond 1.0 mol% did not help to improve photoactivity of the catalyst
289 due to high percentage of free $Fe_2O_3$ ($Fe^{3+}$), which was not incorporated into $TiO_2$ lattice [40].

290 On the other hand, band gap values of $Fe_2O_3$-$TiO_2$ were enhanced considerably as compared to
291 P25 (Table 1 and Fig. 7a). An improvement in band gap values indicated a successful
292 incorporation of $Fe^{3+}$ into the $TiO_2$ framework [40]. Notably, coupling of $Fe_2O_3$ with $TiO_2$
293 stimulated better light harvesting ability and further extended the light absorption range as shown
294 in Fig. 7b. In addition, plot of transformed Kulbeka-Munk function (Fig. 7a) reveals that band
295 gap energy of $Fe_2O_3$-$TiO_2$ was lower (2.95 eV) than P25 (3.35 eV). This observation was
296 probably due to electronic coupling between the wide band gap of $TiO_2$ with the narrow band
297 gap of $Fe_2O_3$ [41].

298 Based on one-way ANOVA, maximum photodegradation efficiency of PPME (62.3% COD
299 removal) was observed at 20 min of milling time, 250 rpm of milling speed, and 1 mol% of
300 $Fe_2O_3$ loading. The synthesized $Fe_2O_3$-$TiO_2$ photocatalyst was 1.5-times more superior to the
301 commercial P25 (40.6% COD removal).

302

303 **3.2. Comparison of other metal oxide-$TiO_2$ photocatalysts with $Fe_2O_3$-$TiO_2$**

304

305 Other metal oxide candidates ($WO_3$, ZnO, and $CeO_2$) were introduced into the $TiO_2$ lattice
306 under recommended milling conditions and their photocatalytic activity was compared with
307 $Fe_2O_3$-$TiO_2$. Based on the photodegradation of PPME (Fig. 9 and Table 4), it was apparent that
308 $Fe_2O_3$-$TiO_2$ attained the highest COD removal (62.3%) as compared to other metal oxide-$TiO_2$
309 photocatalysts (35.4-45.5%), P25 (40.6%), anatase $TiO_2$ (24.9%), rutile $TiO_2$ (2.9%), and $Fe_2O_3$
310 (1.1%). Therefore, $Fe_2O_3$-$TiO_2$ was established as a desired and promising photocatalyst to
311 degrade PPME in this work.

312

### 3.3. Detailed characterizations of $Fe_2O_3$-$TiO_2$

The fabricated $Fe_2O_3$-$TiO_2$ under recommended milling conditions (20 min of milling time, 250 rpm of milling speed, and 1 mol% of $Fe_2O_3$ loading) was subjected to additional characterization studies to further investigate its catalytic properties.

#### 3.3.1. Elemental compositions and distribution

EDX spectrum (Fig. 10a) shows simultaneous presence of Fe, Ti and O elements in $Fe_2O_3$-$TiO_2$, which was produced through mechanochemical process. In addition, EDX mapping (Fig. 10b-d) shows extensive dispersion of Fe and O elements within the $TiO_2$ framework. This result indicated that $Fe_2O_3$ was well distributed throughout the fabricated $Fe_2O_3$-$TiO_2$ using mechanochemical process. Elemental compositions of $Fe_2O_3$-$TiO_2$ sample was further verified using XPS analysis.

In order to ascertain the chemical states of Fe, Ti and O existing in $Fe_2O_3$-$TiO_2$, XPS analysis was conducted. As displayed in Fig. 11a, XPS survey spectrum detected the presence of Fe (Fe 2p), Ti (Ti 2p), and O (O 1s) in $Fe_2O_3$-$TiO_2$. Carbon peak (C 1s) was attributed to the carbon tape used as a support during XPS analysis. High resolution XPS spectra reveal chemical species within the prepared $Fe_2O_3$-$TiO_2$ (Fig. 11b-d). Binding energies of Fe $2p_{3/2}$ and Fe $2p_{1/2}$ were 710.7 and 724.5 eV respectively, verifying the presence of $Fe^{3+}$. An absence of peaks around 707 and 719 eV ruled out the presence of $Fe^{2+}$, firmly supporting the addition of $\gamma$-$Fe_2O_3$ phase into $TiO_2$ [42]. Peaks corresponding to $Ti^{4+}$ were centered at 458.6 and 464.4 eV, which were analogous to Ti $2p_{3/2}$ and Ti $2p_{1/2}$, respectively. From O 1s spectra, binding energy at 529.8

335 eV was assigned to lattice oxygen, $O^{2-}$ species from $Fe_2O_3$ and Ti-O-Ti [34,43]. The attained XPS
336 findings (Fig. 11a-d) were in conformity with the obtained EDX analysis data (Fig. 10a).
337
338 **3.3.2. Surface morphology**
339 TEM image (Fig. 12a) shows that $Fe_2O_3$-$TiO_2$ nanoparticles had an average particle size of
340 30 nm. Darker regions corresponded to $Fe_2O_3$ particles whereas lighter regions were ascribed to
341 $TiO_2$ nanoparticles. Noticeably, an intimate contact between $Fe_2O_3$ and $TiO_2$ particles was
342 formed from mechanochemical process. The contact was advantageous for charge transfer
343 between the two metal oxides due to a shorter carrier diffusion length that would suppress
344 recombination of electron-hole pairs [37]. Furthermore, $Fe_2O_3$ particles appeared to be well-
345 dispersed throughout the $Fe_2O_3$-$TiO_2$ sample. High resolution TEM (HRTEM) image (Fig. 12b)
346 revealed clear lattice fringes of $Fe_2O_3$ and $TiO_2$. Lattice fringe of 0.29 nm was equivalent to
347 (220) plane of γ-$Fe_2O_3$, whereas lattice fringes of 0.35 and 0.32 nm corresponded to (101)
348 anatase plane and (110) rutile plane of $TiO_2$, respectively [43,44].
349
350 **3.3.3. Raman analysis**
351 Based on Raman spectrum of the $Fe_2O_3$-$TiO_2$ sample (Fig. 13), major Raman peaks at 155,
352 394, 514, and 633 $cm^{-1}$ were indexed to the typical structure of $TiO_2$ whereas peak at 205 $cm^{-1}$
353 indicated the presence of γ-$Fe_2O_3$ [35,45]. A formation of Fe-O-Ti bond in the fabricated $Fe_2O_3$-
354 $TiO_2$ was evidenced by a peak at 279 $cm^{-1}$. This denoted that $Fe^{3+}$ replaced some $Ti^{4+}$ species in
355 lattice sites of the crystalline structure, indicating a successful synthesis of $Fe_2O_3$-$TiO_2$
356 photocatalyst [35]. Peak intensity analogous to the presence of $Fe_2O_3$ was low due to low
357 concentration of $Fe_2O_3$ (1 mol%). An incorporation of Fe atoms into Ti lattice sites also caused a

358 shift of peaks to slightly greater frequencies as a result from force constant and vibrational
359 amplitudes of neighbouring bonds [34,35].
360
361 **3.3.4. FTIR analysis**
362 FTIR analysis was employed to determine the functional groups present in $Fe_2O_3$-$TiO_2$ [21].
363 Based on Fig. 14, FTIR spectrum of $Fe_2O_3$-$TiO_2$ was similar to P25, signifying that $Fe_2O_3$ was
364 well-infused into the $TiO_2$ lattice [39]. Two bands observed at 3400 and 1634 $cm^{-1}$ were
365 characteristics of O-H stretching vibrations and H-OH bending of hydroxyl groups present [46].
366 These bands played a significant role in photocatalytic reactions to react with photogenerated
367 holes on the $Fe_2O_3$-$TiO_2$ surface upon light irradiation. Broad peak at 3250 $cm^{-1}$ was due to O-H
368 stretching vibration of water whereas bands at 2924 and 2840 $cm^{-1}$ were attributed to C-H
369 stretching vibrations of alkyl chain [40,42].
370
371
372 **4. Conclusions**
373
374 In this study, a photoactive $Fe_2O_3$-$TiO_2$ catalyst was successfully synthesized using a one-
375 step facile and solvent-free mechanochemical process under ambient temperature and
376 atmospheric pressure. Characterization studies showed that the synthesized $Fe_2O_3$-$TiO_2$
377 possessed crystalline structures of γ-$Fe_2O_3$, anatase, and rutile phases of $TiO_2$. It was further
378 confirmed that Fe, Ti and O elements were present and were well-dispersed within the $Fe_2O_3$-
379 $TiO_2$ framework. Enhanced photoactivity of $Fe_2O_3$-$TiO_2$ was attributed to the following
380 distinctive traits: (i) formation of Fe-O-Ti bond due to substitution of $Ti^{4+}$ by $Fe^{3+}$ in $TiO_2$ lattice;

(ii) higher specific surface area (58.40 $m^2/g$) and porosity (0.29 $cm^3/g$) than commercial P25; (iii) lower band gap (2.95 eV) than P25 due to electronic coupling of $TiO_2$ and $Fe_2O_3$; (iv) and suppressed electron-hole recombination rate, which was ascribed to the incorporation of $Fe^{3+}$ that acted as a charge-transfer mediator. In addition, the highest treatment efficiency of PPME (62.3% of COD removal) was achieved by using $Fe_2O_3$-$TiO_2$, which was synthesized at 20 min of milling time, 250 rpm of milling speed, and 1 mol% of $Fe_2O_3$ loading. Markedly, the photoactivity of $Fe_2O_3$-$TiO_2$ was 53.4% higher than the commercial P25. In conclusion, this study provided a better insight into the potential use of mechanochemical process as a greener, simpler and low-cost approach in synthesizing high efficiency photocatalysts to degrade complex industrial effluent.

**Acknowledgements**

The authors would like to thank Monash University Malaysia for providing W. Subramonian with a Ph.D. scholarship.

396 **References**

397 [1] C.Y. Teh, P.M. Budiman, K.P.Y. Shak, T.Y. Wu, Recent advancement of coagulation-
398 flocculation and its application in wastewater treatment, Ind. Eng. Chem. Res. 55 (2016)
399 4363-4389.
400 [2] L. Fernandes, M.S. Lucas, M.I. Maldonado, I. Oller, A. Sampaio, Treatment of pulp mill
401 wastewater by *Crytococcus* podzolicus and solar photo-Fenton: a case study, Chem. Eng. J.
402 245 (2014) 158-165.
403 [3] W. Subramonian, T.Y. Wu, Effect of enhancers and inhibitors on photocatalytic sunlight
404 treatment of methylene blue, Water Air Soil Pollut. 225 (2014) 1-15.
405 [4] C. Lopez-Lopez, J. Martín-Pascual, M.V. Martínez-Toledo, M. M. Muñío, E. Hontoria,
406 J.M. Poyatos, Kinetic modeling of TOC removal by $H_2O_2$/UV, photo-Fenton and
407 heterogeneous photocatalysis processes, Int. J. Environ. Sci. Technol. 12 (2016) 3255-3262.
408 [5] H.N. Chin, Z.Z. Noor, N.S.A. Mutamin, K.L. Chi, Green Technology in wastewater
409 treatment technologies: integration of membrane bioreactor with various wastewater
410 treatment systems, Chem. Eng. J. 283 (2016) 582-594.
411 [6] E. Ghasemi, H. Ziyadi, A.M. Afshar, M. Sillanpää, Iron oxide nanofibers: a new magnetic
412 catalyst for azo dyes degradation in aqueous solution, Chem.
413 Eng. J. 264 (2015) 146-151.
414 [7] D. Wodka, R.P. Socha, E. Bielańska, M. Elżbieciak-Wodka, P. Nowak, P. Warszyński,
415 Photocatalytic activity of titanium dioxide modified by $Fe_2O_3$ nanoparticles, Appl. Surf. Sci.
416 319 (2014) 173-180.
417 [8] J.O. Carneiro, S. Azevedo, F. Fernandes, E. Freitas, M. Pereira, C.J. Tavares, S. Lanceros-
418 Méndez, V. Teixeira, Synthesis of iron-doped $TiO_2$ nanoparticles by ball-milling process:

the influence of process parameters on the structural, optical, magnetic, and photocatalytic properties, J. Mater. Sci. 49 (2014) 7476-7488.

[9] Y. Su, Z. Wu, Y. Wu, J. Yu, L. Sun, C. Lin, Acid orange II degradation through a heterogeneous Fenton-like reaction using Fe-$TiO_2$ nanotube arrays as a photocatalyst, J. Mater. Chem. A. 3 (2015) 8537-8544.

[10] F.C.F. Low, T.Y. Wu, C.Y. Teh, J.C. Juan, N. Balasubramanian, Investigation into photocatalytic decolorisation of CI Reactive Black 5 using titanium dioxide nanopowder, Color. Technol. 128 (2012) 44-50.

[11] D. Liŭ, Z. Li, W. Wang, G. Wang, D. Liú, Hematite doped magnetic $TiO_2$ nanocomposites with improved photocatalytic activity, J. Alloy. Compd. 654 (2016) 491-497.

[12] S. Neubert, D. Mitoraj, S.A. Shevlin, P. Pulisova, M. Heimann, Y. Du, G.K.L. Goh, M. Pacia, K. Kruczata, S. Turner, W. Macyk, Z.X. Guo, R.K. Hocking, R. Beranek, Highly efficient rutile $TiO_2$ photocatalysts with single Cu(II) and Fe(III) surface catalytic sites, J. Mater. Chem. A. 4 (2016) 3127-3138.

[13] A. Luengnaruemitchai, K. Srihamat, C. Pojanavaraphan, R. Wanchanthuek, Activity of Au/$Fe_2O_3$-$TiO_2$ catalyst for preferential CO oxidation, Int. J. Hydrog. Energy 40 (2015) 13443-13455.

[14] S. Zhang, Q. Zhong, Y. Shen, L. Zhu, J. Ding, New insight into the promoting role of process on the $CeO_2$-$WO_3$/$TiO_2$ catalyst for NO reduction with $NH_3$ at low-temperature, J. Colloid Interface Sci. 448 (2015) 417-426.

[15] M. Naimi-Joubani, M. Shirzad-Siboni, J.-K. Yang, M. Gholami, M. Farzadkia, Photocatalytic reduction of hexavalent chromium with illuminated ZnO/$TiO_2$ composite, J. Ind. Eng. Chem. 22 (2015) 317-323.

[16] K.-R. Wee, B.D. Sherman, M.K. Brennaman, M.V. Sherridan, A. Nayak, L. Alibabaei, T.J. Meyer, An aqueous, organic dye derivated $SnO_2/TiO_2$ core/shell photoanode, J. Mater. Chem. A 4 (2016) 2969-2975.

[17] W. Deng, Q. Dai, Y. Lao, B. Shi, X. Wang, Low temperature catalytic combustion of 1,2-dichlorobenzene over $CeO_2$-$TiO_2$ mixed oxide catalysts, Appl. Catal. B-Environ. 181 (2016) 848-861.

[18] S. Fathinia, M. Fathinia, A.A. Rahmani, A. Khataee, Preparation of natural pyrite nanoparticles by high energy planetary ball milling as a nanocatalyst for heterogeneous Fenton process, Appl. Surf. Sci. 327 (2015) 190-200.

[19] C.Y. Teh, T.Y. Wu, J.C. Juan, Facile sonochemical synthesis of N,Cl-codoped $TiO_2$: synthesis effects, mechanism and photocatalytic performance, Catal. Today 256 (2015) 365-374.

[20] K. Wieczorek-Ciurowa, K. Gamrat, Mechanochemical synthesis as an example of green processes, J. Therm. Anal. Calorim. 88 (2007) 213-217.

[21] Ž. Kesić, I. Lukić, M. Zdujić, Č. Jovalekić, H. Liu, D. Skala, Mechanochemical synthesis of $CaO{\cdot}ZnO{\cdot}K_2CO_3$ catalyst: characterization and activity for methanolysis of sunflower oil, Chem. Ind. Chem. Eng. 21 (2015) 1-12.

[22] S. Lu, J. Huang, Z. Peng, X., Li, J. Yan, Ball-milling 2,4,6-trichlorophenol with calcium oxide: dechlorination experiment and mechanism considerations, Chem. Eng. J. 195-196 (2012) 62-68.

[23] K. Ralphs, C. Hardacre, S.L. James, Application of heterogeneous catalyst prepared by mechanochemical synthesis, Chem. Soc. Rev. 42 (2013) 7701-7718.

[24] A. Banerjee, R. Gupta, K. Balani, Non-monotonic lattice parameter variation in ball-milled ceria, J. Mater. Sci. 50 (2015) 6349-6358.

[25] C. Xu, S. De, A.M. Balu, M. Ojeda, R. Luque, Mechanochemical synthesis of advanced nanomaterials for catalytic applications, Chem. Commun. 15 (2015) 6698-6713.

[26] T.J. Clarke, T.E. Davies, S.A. Kondrat, S.H. Taylor, Mechanochemical synthesis of copper manganese oxide for the ambient temperature oxidation of carbon monoxide, Appl. Catal. B-Environ. 165 (2015) 222-231.

[27] W. Subramonian, T.Y. Wu, S.-P. Chai, A comprehensive study on coagulant performance and floc characterization of natural *Cassia obtusifolia* seed gum in treatment of raw pulp and paper mill effluent, Ind. Crops Prod. 61 (2014) 317-324.

[28] W. Subramonian, T.Y. Wu, S.-P. Chai, An application of response surface methodology for optimizing coagulation process of raw industrial effluent using *Cassia obtusifolia* seed gum together with alum, Ind. Crops Prod. 70 (2015) 107-115.

[29] S.D. House, J.J Vajo, C. Ren, A.A. Rockett, I.M. Robertson, Effect of ball milling duration and dehydrogenation on the morphology, microstructure and catalyst dispersion in Ni-catalyzed $MgH_2$ hydrogen storage materials, Acta Mater. 86 (2015) 55-68.

[30] X. Chen, T. Lu, Z. Lu, L. Chen, Q. Zhang, G. Cheng, J. Qi, Systematic optimization of ball-milling for highly transparent Yb:YAG ceramic using co-precipitated raw powders, J. Alloy. Compd. 653 (2015) 552-560.

[31] Y.H. Taufiq-Yap, C.K. Goh, G.J. Hutchings, N. Dummer, J.K. Bartley, Effects of mechanochemical treatment to the vanadium phosphate catalysts derived from $VOPO_4{\cdot}2H_2O$, J. Mol. Catal. A-Chem. 260 (2006) 24-31.

[32] F.M.T. Mendes, A.C.C. Marques, D.L. Mendonça, M.S. Oliveira, R.O. Moutta, V.S. Ferreira-Leitão, High surface area activated carbon from sugar cane straw, Waste Biomass Valor. 6 (2015) 433-440.

[33] N. Aman, N.N. Das, T. Mishra, Effect of N-doping on visible light activity of $TiO_2$-$SiO_2$ mixed oxide photocatalysts, J. Environ. Chem. Eng. 4 (2016) 191-196.

[34] L. Qin, X. Pan, L. Wang, X. Sun, G. Zhang, X. Guo, Facile preparation of mesoporous $TiO_2$ (B) nanowires with well-dispersed $Fe_2O_3$ nanoparticles and their photochemical catalytic behavior, Appl. Catal. B-Environ. 150-151 (2014) 544-553.

[35] A. Banisharif, A.A. Khodadadi, Y. Mortszavi, A.A. Firooz, J. Behestian, S. Agah, S. Menbari, Highly active $Fe_2O_3$-doped $TiO_2$ photocatalyst for degradation of trichloroethylene in air under UV and visible light irradiation: experimental and computational studies, Appl. Catal. B-Environ. 165 (2015) 209-221.

[36] W. Li, X. Liu, H. Li, Hydrothermal synthesis of graphene/$Fe^{3+}$ -doped $TiO_2$ nanowire composites with highly enhanced photocatalytic activity under visible light irradiation, J. Mater. Chem. A 3 (2015) 15214-15224.

[37] S.J.A. Moniz, S.A. Shevlin, X. An, Z.-X. Guo, J. Tang, $Fe_2O_3$-$TiO_2$ nanocomposites for enhanced charge separation and photocatalytic activity, Chem. Eur. J. 20 (2014) 15571-15579.

[38] G.S. Pozan, M. Isleyen, S. Gokcen, Transition metal coated $TiO_2$ nanoparticles: synthesis, characterization and their photocatalytic activity, Appl. Catal. B-Environ. 140-141 (2013) 537-545.

507 [39] T.K. Ghorai, M. Chakraborty, P. Pramanik, Photocatalytic performance of nano-
508 photocatalyst from $TiO_2$ and $Fe_2O_3$ by mechanochemical synthesis, J. Alloy. Compd. 509
509 (2011) 8158-8164.
510 [40] B. Palanisamy, C.M. Babu, B. Sundaravel, S. Anandan, V. Murugesan, Sol-gel synthesis of
511 mesoporous mixed $Fe_2O_3/TiO_2$ photocatalyst: application for degradation of 4-chlorophenol,
512 J. Hazard. Mater. 252-253 (2013) 233-242.
513 [41] Y. Wang, X. Fan, S. Wang, G. Zhang, F. Zhang, Magnetically separable γ-$Fe_2O_3/TiO_2$
514 nanotubes for photodegradation of aqueous methyl orange, Mater. Res. Bull. 48 (2013) 785-
515 789.
516 [42] M.A. Bhosale, D. Ummineni, T. Sasaki, D. Nishio-Hamane, B.M. Bhanage, Magnetically
517 separable γ-$Fe_2O_3$ nanoparticles: an efficient catalyst for acrylation of alcohols, phenols, and
518 amines using sonication energy under solvent free condition, J. Mol. Catal. A-Chem. 404-
519 405 (2015) 8-17.
520 [43] G. Wu, Y. Cheng, Y. Ren, Y. Wang, Z. Wang, H. Wu, Synthesis and characterization of γ-
521 $Fe_2O_3$@C nanorod-carbon sphere composite and its application as microwave absorbing
522 material, J. Alloy. Compd. 652 (2015) 346-350.
523 [44] P. Mirtchev, K. Liao, E. Jaluague, Q. Qiao, Y. Tian, M. Varela, K.S. Burch, S.J. Pennycook,
524 D.D. Perovic, G. Ozin, $Fe_2O_3/Cu_2O$ heterostructured nanocrystals, J. Mater. Chem. A 2
525 (2014) 8525-8533.
526 [45] M.T. Qamar, M. Aslam, I.M.I. Ismail, N. Salah, A. Hameed, The assessment of the
527 photocatalytic activity of magnetically retrievable ZnO coated γ–$Fe_2O_3$ in sunlight exposure,
528 Chem. Eng. J. 283 (2016) 656-667.

529 [46] Z.Y. Bai, Q. Yang, J.L. Wang, $Fe_3O_4$/multi-walled carbon nanotubes as an efficient catalyst
530 for catalyst for catalytic ozonation of p-hydroxybenzoic acid, Int. J. Environ. Sci. Technol.
531 13 (2016) 483-492.

**List of Figures**

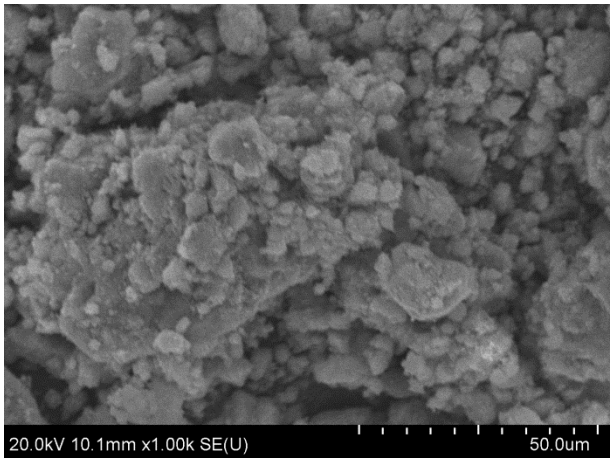


**Fig. 1. (a)**

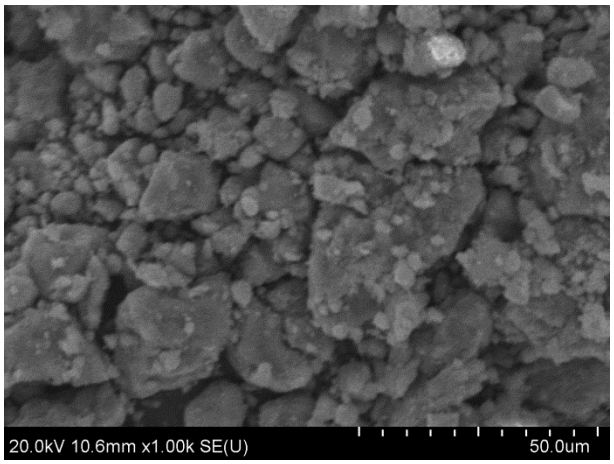


**Fig. 1. (b)**

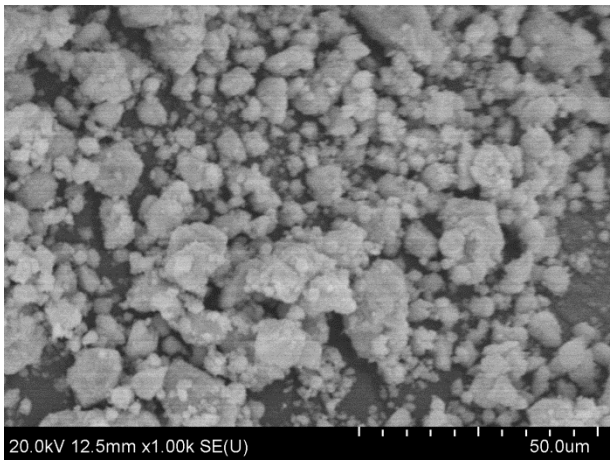


**Fig. 1. (c)**

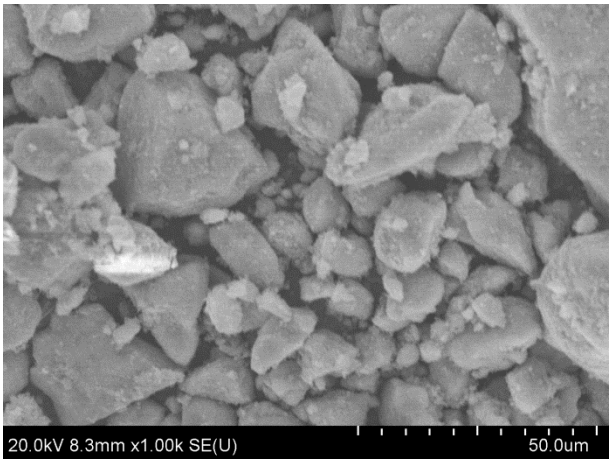


**Fig. 1. (d)**

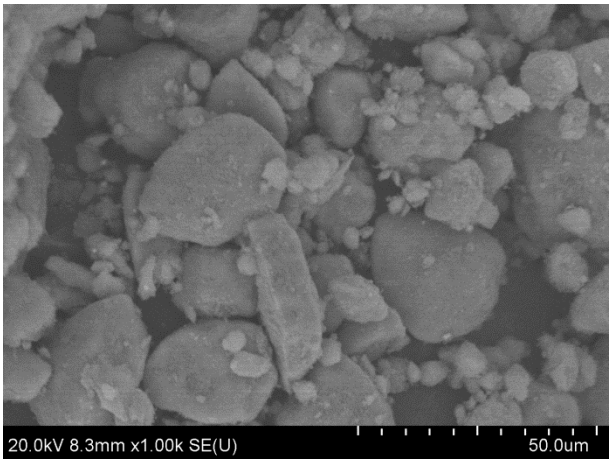


**Fig. 1. (e)**

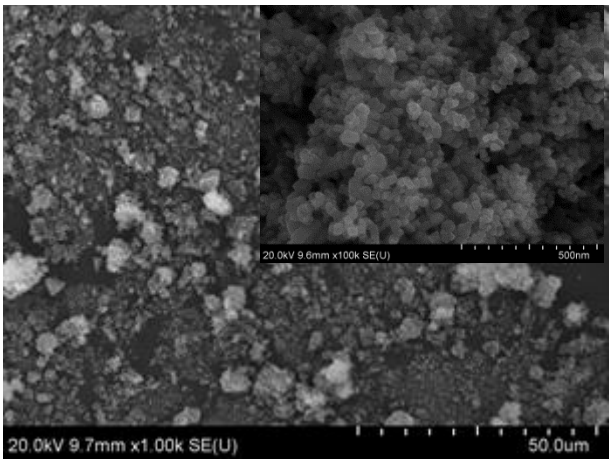


**Fig. 1. (f)**

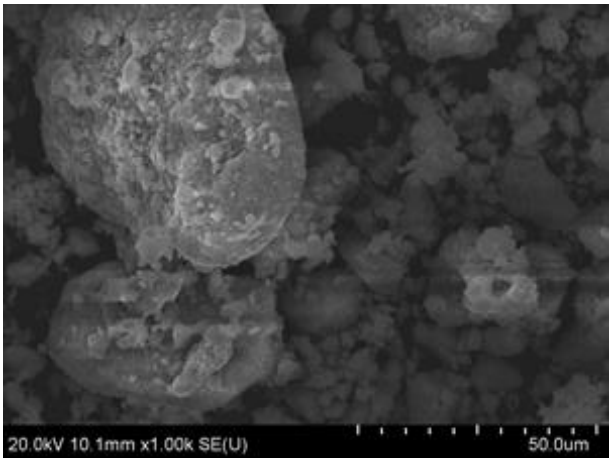


**Fig. 1. (g)**

**Fig. 1.** FESEM images of (a) $Fe_2O_3$-$TiO_2$ milled at 10 min, (b) 15 min, (c) 20 min, (d) 25 min and (e) 30 min, (f) P25 and (g) $Fe_2O_3$.

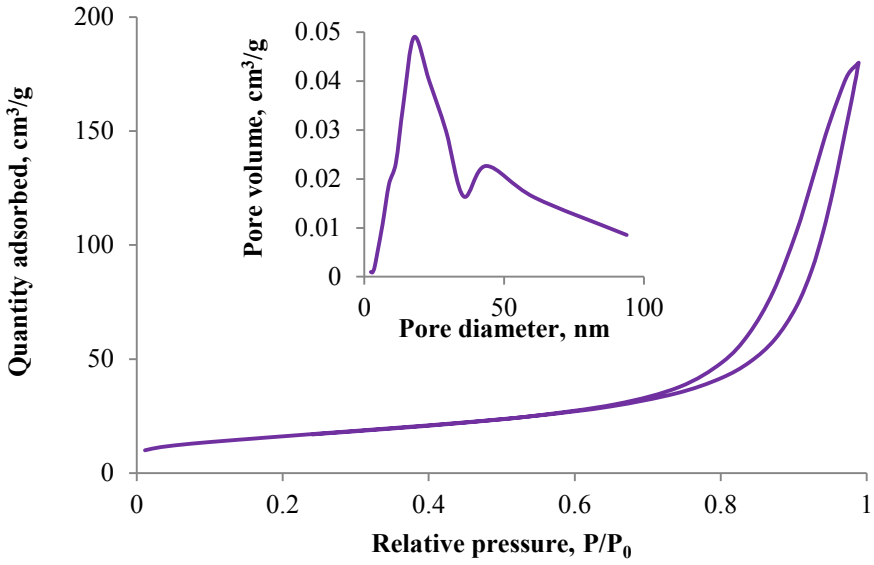


**Fig. 2.** Nitrogen adsorption/desorption isotherm. Inset shows the BJH pore size distribution of $Fe_2O_3$-$TiO_2$.

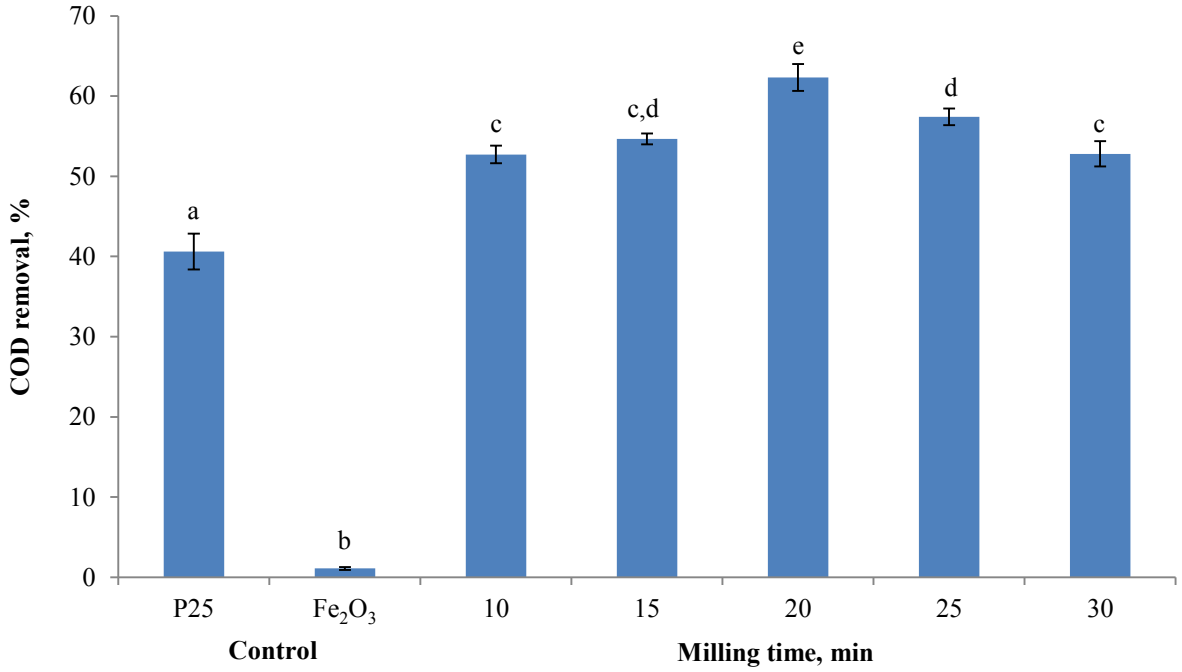


**Fig. 3.** Effect of milling time on photodegradation of PPME (milling speed = 250 rpm; [$Fe_2O_3$] = 1 mol%; ball:powder mass ratio = 10:1; irradiation time = 3 h; initial effluent pH = 4; [$Fe_2O_3$-$TiO_2$] = 1.0 g/L; air

flow rate = 4.0 L/min; $n$ = 3). Values annotated with different letters represent significant differences (one-way ANOVA, Tukey's test; P <0.05).

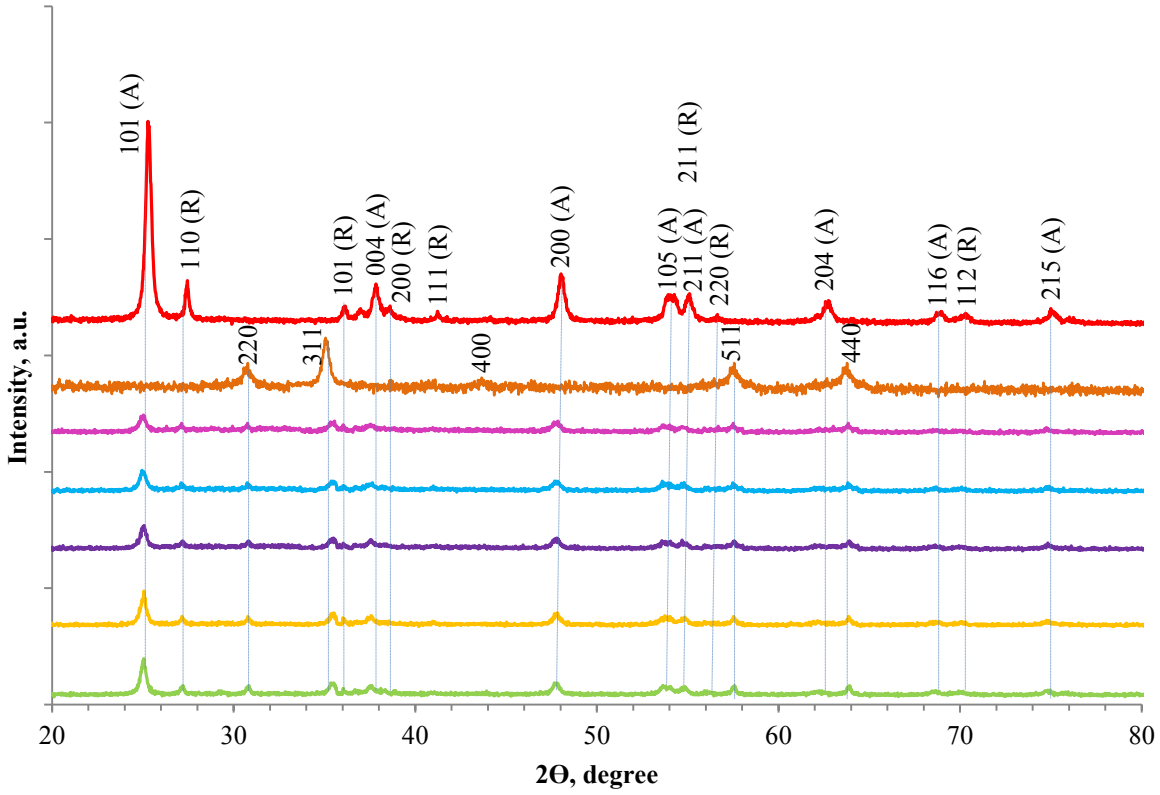


**Fig. 4.** XRD patterns of P25 (red), $Fe_2O_3$ (brown), and $Fe_2O_3$-$TiO_2$ milled at 150 rpm (green), 200 rpm (yellow), 250 rpm (purple), 300 rpm (blue) and 350 rpm (pink) (A: anatase phase; R: rutile phase).

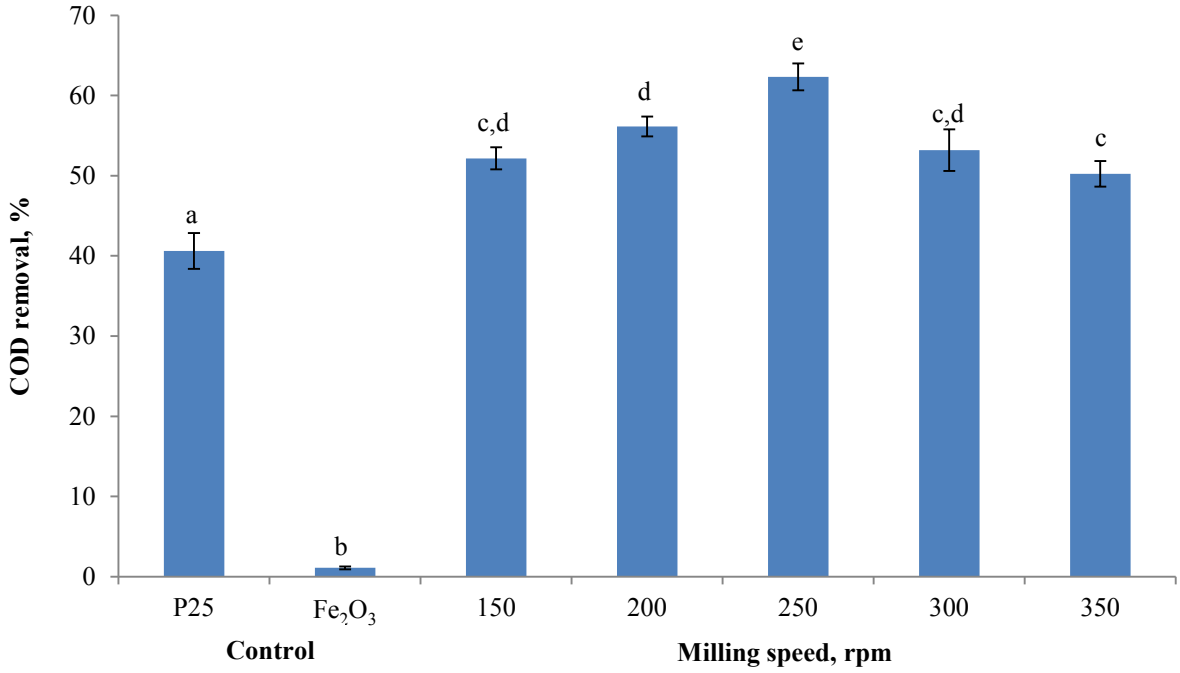


**Fig. 5.** Effect of milling speed on photodegradation of PPME (milling time = 20 min; [$Fe_2O_3$] = 1 mol%; ball:powder mass ratio = 10:1; irradiation time = 3 h; initial effluent pH = 4; [$Fe_2O_3$-$TiO_2$] = 1.0 g/L; air flow rate = 4.0 L/min; $n$ = 3). Values annotated with different letters represent significant differences (one-way ANOVA, Tukey's test; $P < 0.05$).

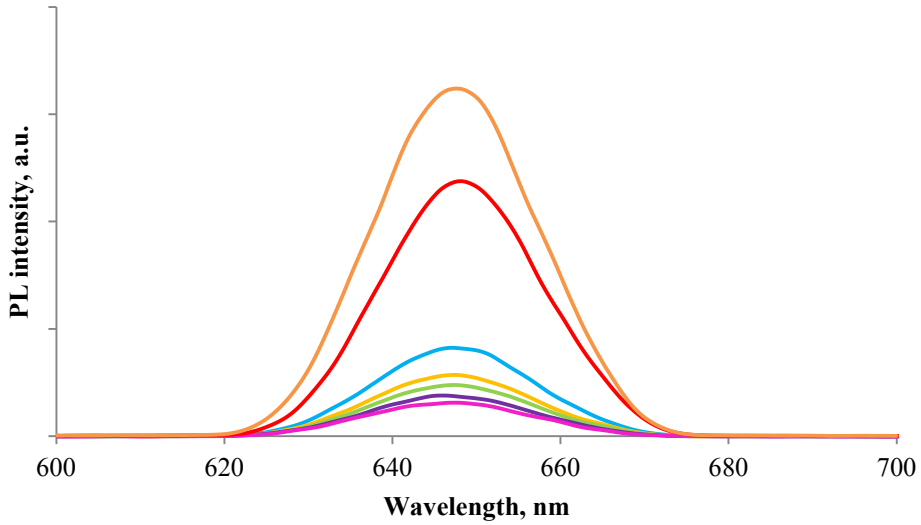


**Fig. 6.** PL spectra of P25 (red), $Fe_2O_3$ (brown), and $Fe_2O_3$-$TiO_2$ with $Fe_2O_3$ loading of 0.4 mol% (blue), 0.6 mol% (yellow), 0.8 mol% (green), 1.0 mol% (purple) and 1.2 mol% (pink).

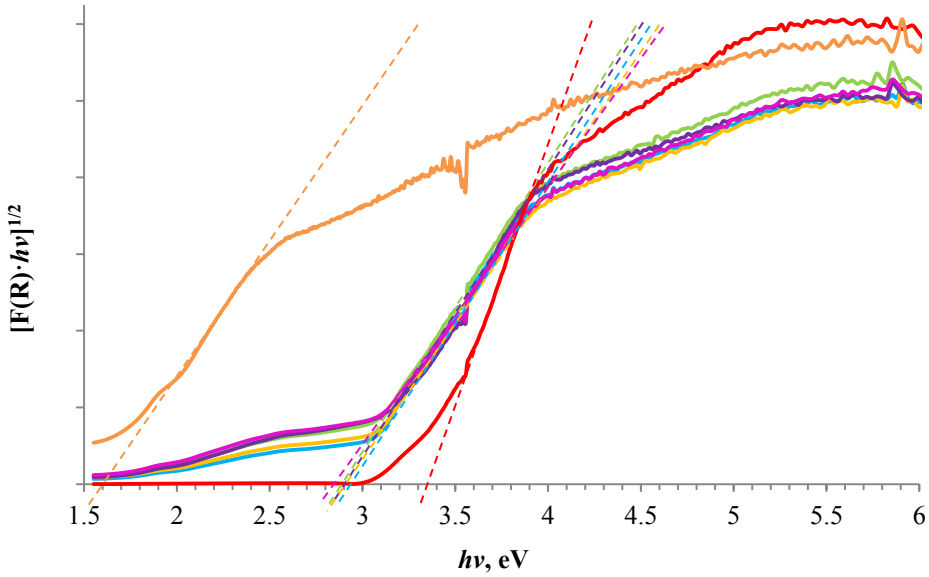


**Fig. 7. (a)**

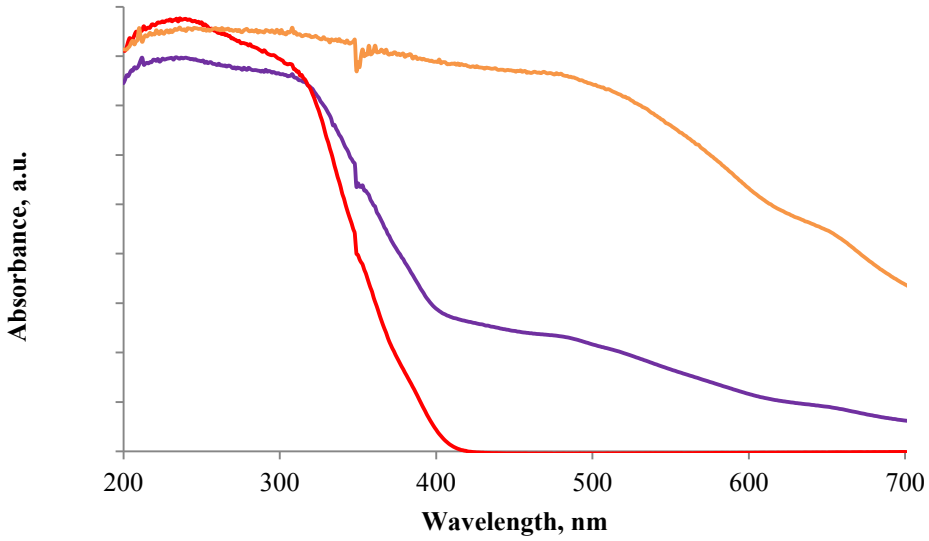


**Fig. 7. (b)**

**Fig. 7.** (a) Plot of transformed Kulbeka-Munk function $[F(R)\cdot h\nu]^{1/2}$ versus $h\nu$ of P25 (red), $Fe_2O_3$ (brown), and $Fe_2O_3$-$TiO_2$ with $Fe_2O_3$ loading of 0.4 mol% (blue), 0.6 mol% (yellow), 0.8 mol% (green), 1.0 mol% (purple) and 1.2 mol% (pink). (b) DRS spectra of P25 (red), $Fe_2O_3$ (brown), and $Fe_2O_3$-$TiO_2$ with $Fe_2O_3$ loading 1.0 mol% (purple).

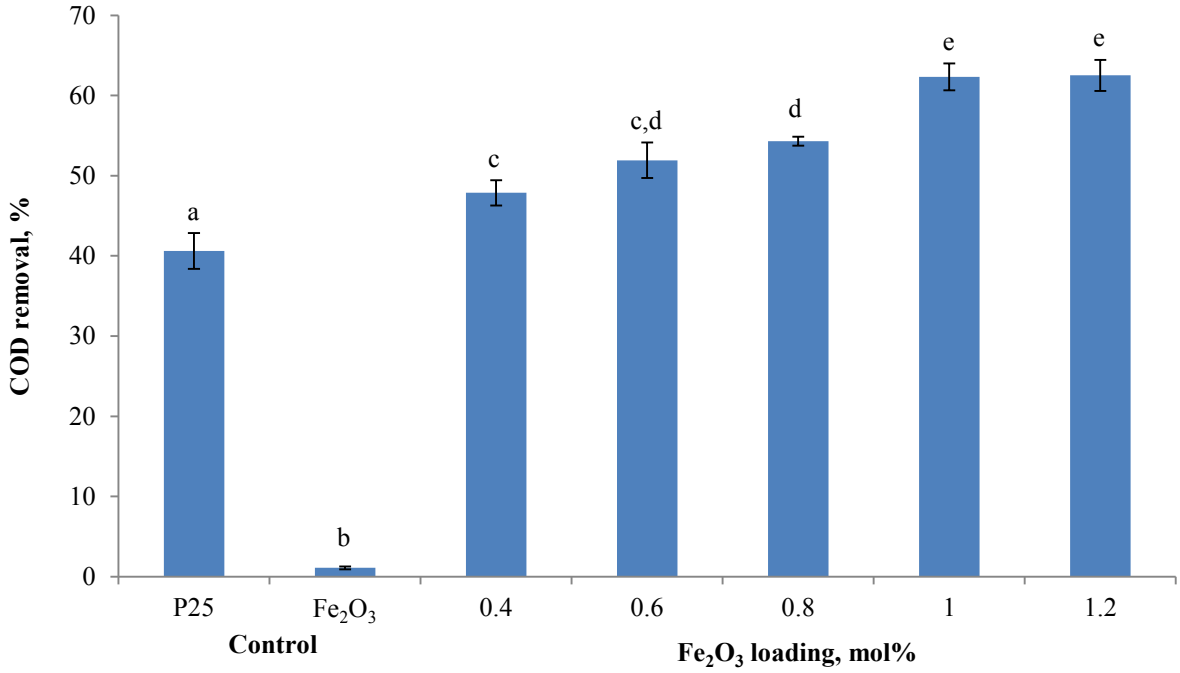


**Fig. 8.** Effect of $Fe_2O_3$ loading on photodegradation of PPME (milling time = 20 min; milling speed = 250 rpm; ball:powder mass ratio = 10:1; irradiation time = 3 h; initial effluent pH = 4; [$Fe_2O_3$-$TiO_2$] = 1.0 g/L; air flow rate = 4.0 L/min; *n* = 3). Values annotated with different letters represent significant differences (one-way ANOVA, Tukey's test; P <0.05).

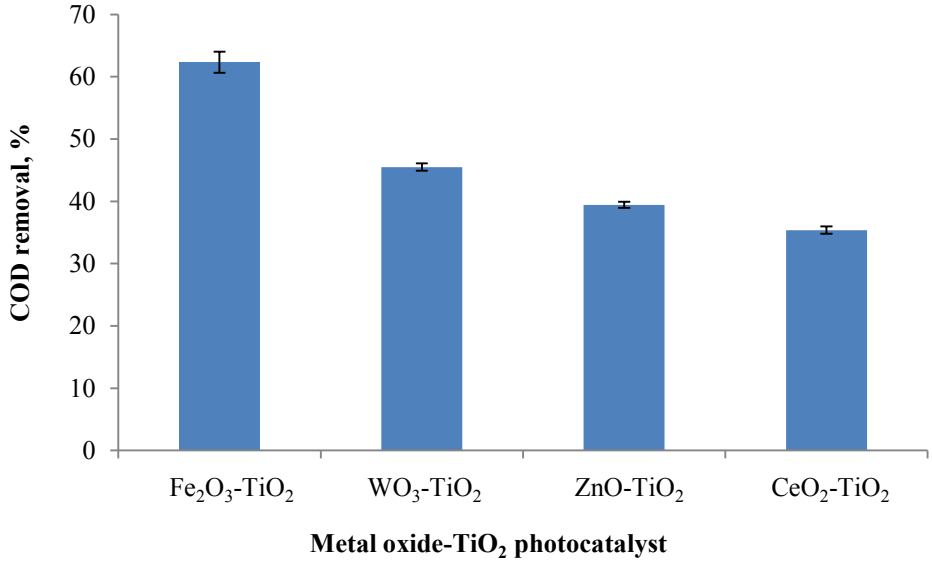


**Fig. 9.** Comparison of other metal oxide-$TiO_2$ photocatalysts with $Fe_2O_3$-$TiO_2$.

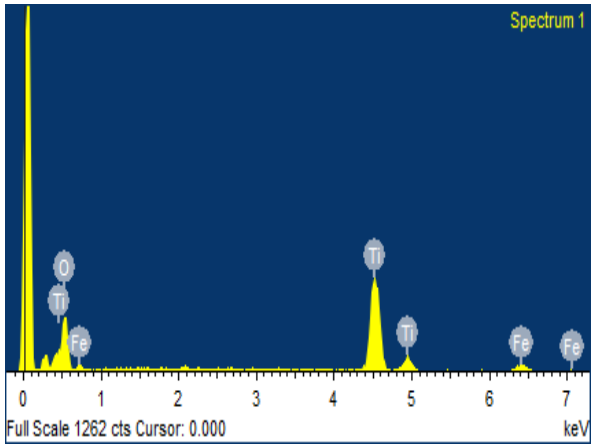


**Fig. 10. (a)**

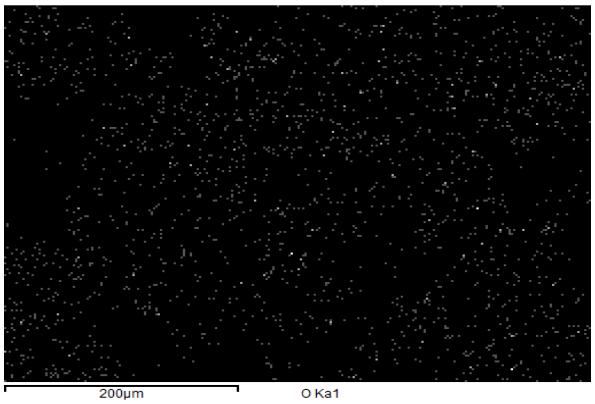


**Fig. 10. (b)**

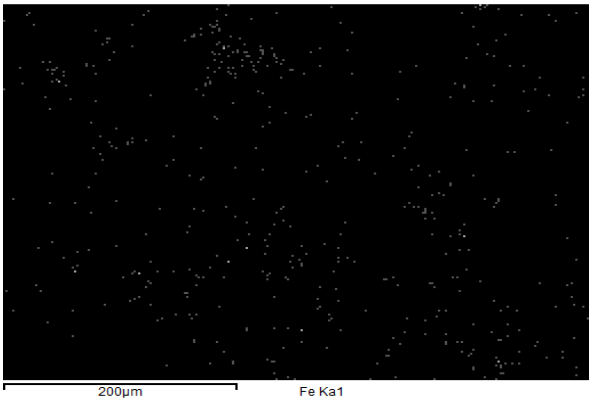


**Fig. 10. (c)**

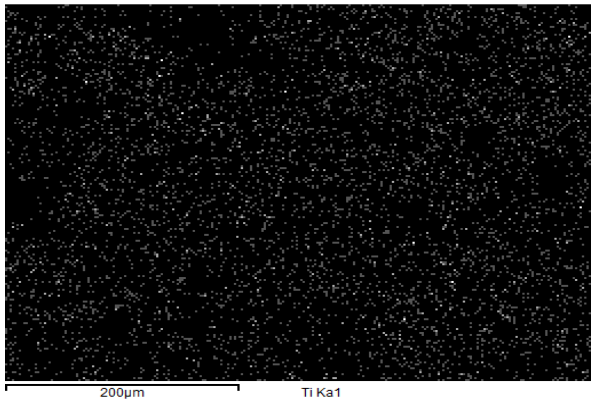


**Fig. 10. (d)**

**Fig. 10.** (a) EDX spectrum of $Fe_2O_3$-$TiO_2$. EDX mapping of (b) O, (c) Fe, and (d) Ti elements in $Fe_2O_3$-$TiO_2$.

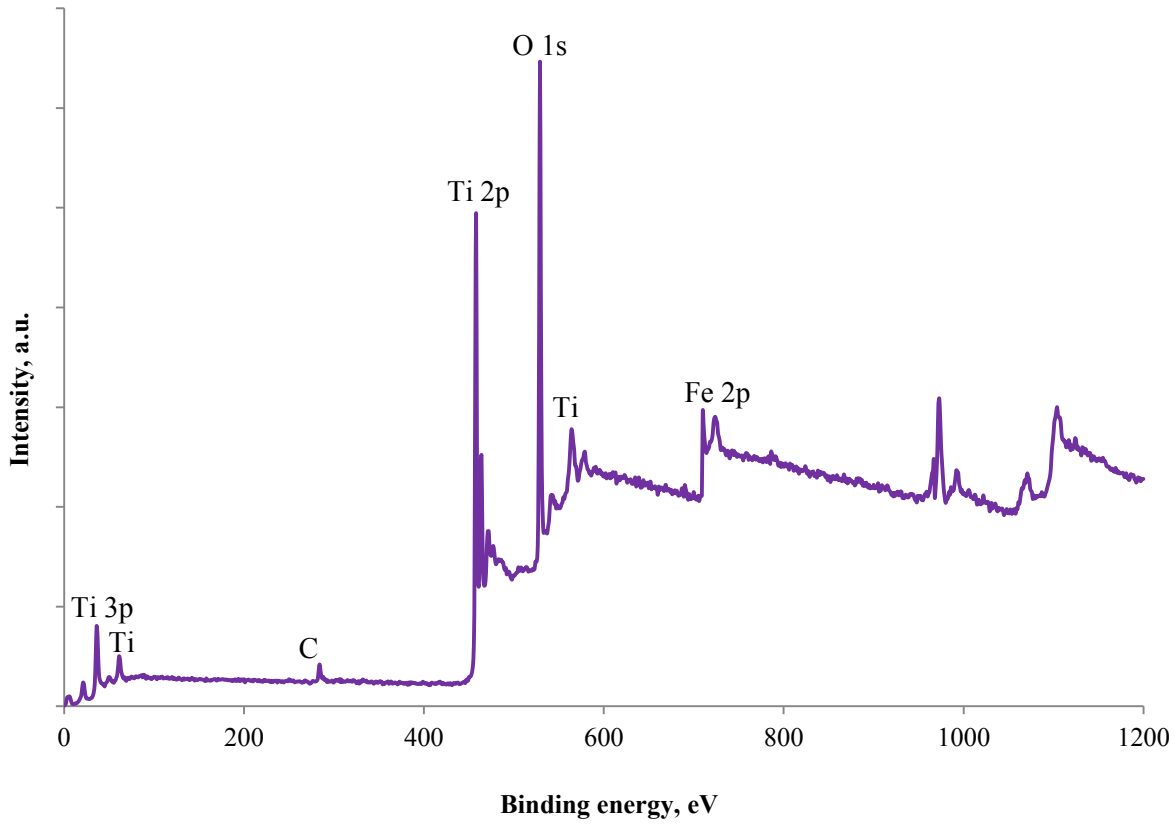


**Fig. 11. (a)**

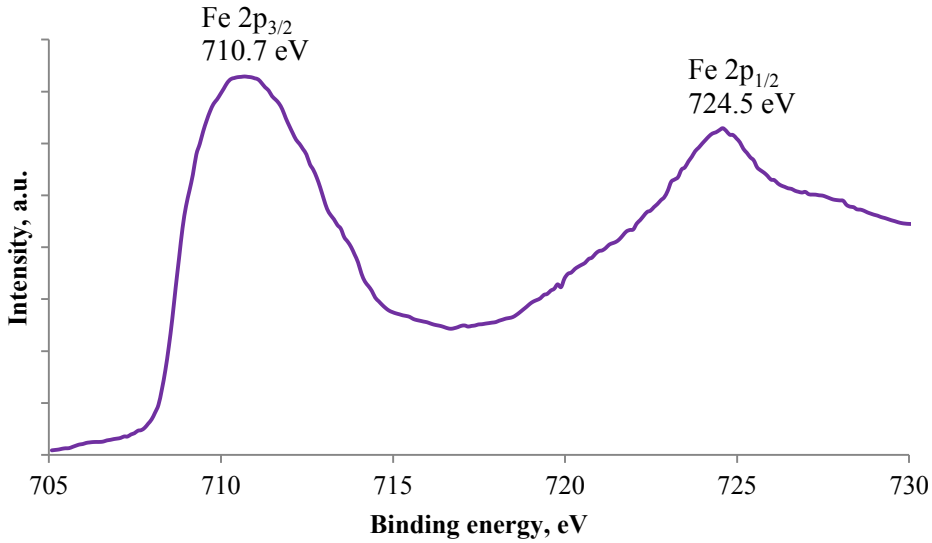


**Fig. 11. (b)**

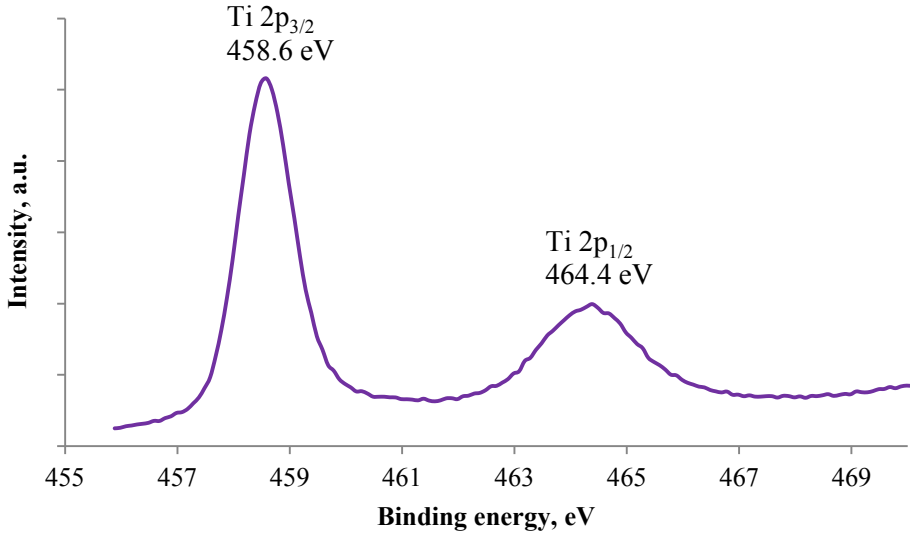


**Fig. 11. (c)**

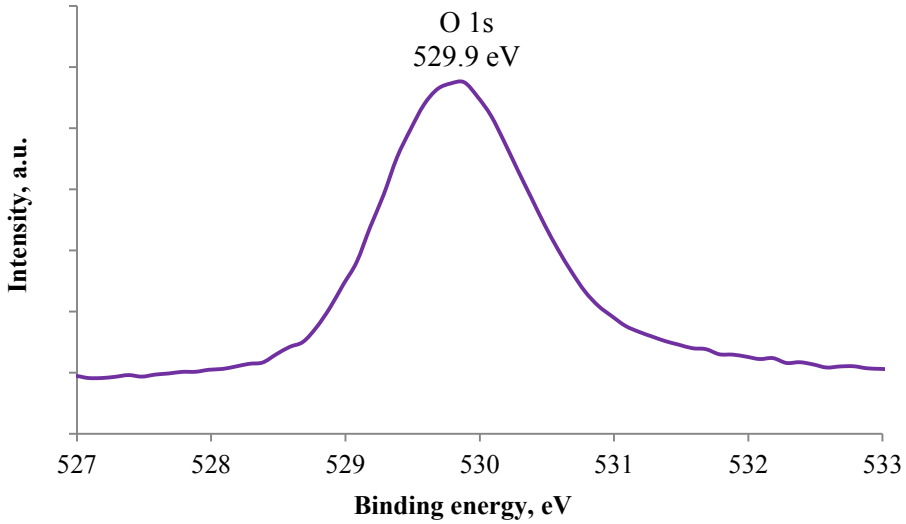


**Fig. 11. (d)**

**Fig. 11.** XPS (a) survey spectrum and narrow spectra of (b) Fe 2p, (c) Ti 2p, and (d) O 1s of $Fe_2O_3$-$TiO_2$.

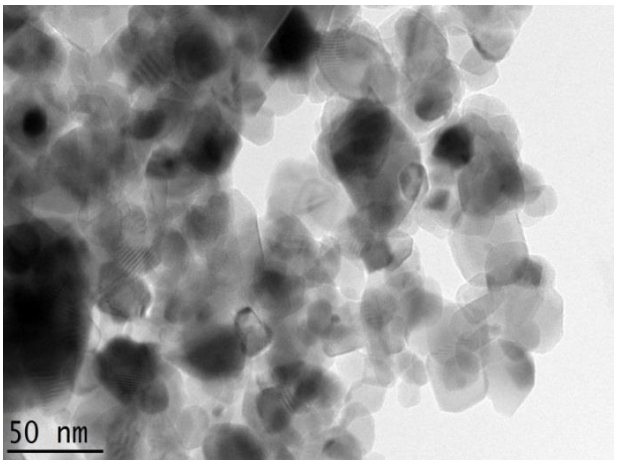


**Fig. 12. (a)**

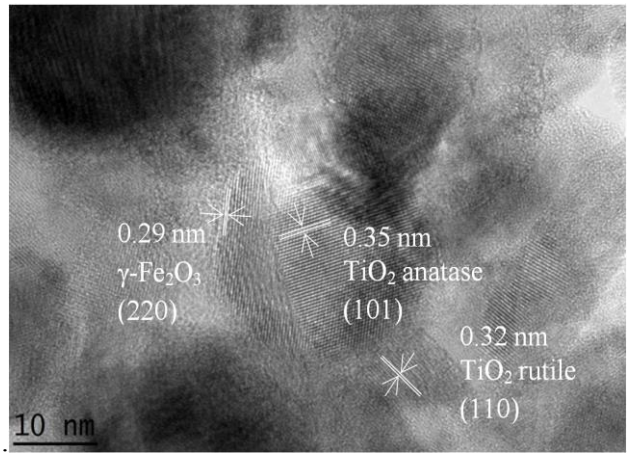


**Fig. 12. (b)**

**Fig. 12.** (a) TEM image of $Fe_2O_3$-$TiO_2$. (b) HRTEM image of $Fe_2O_3$-$TiO_2$.

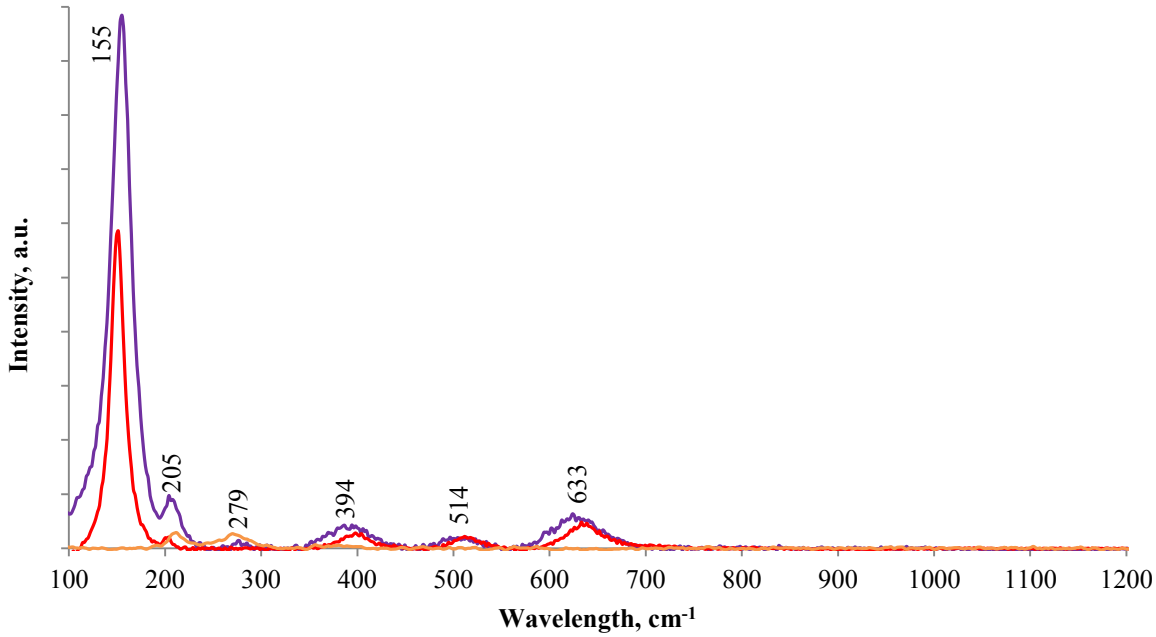


**Fig. 13.** Raman spectra of $Fe_2O_3$-$TiO_2$ (purple), P25 (red), and $Fe_2O_3$ (brown).

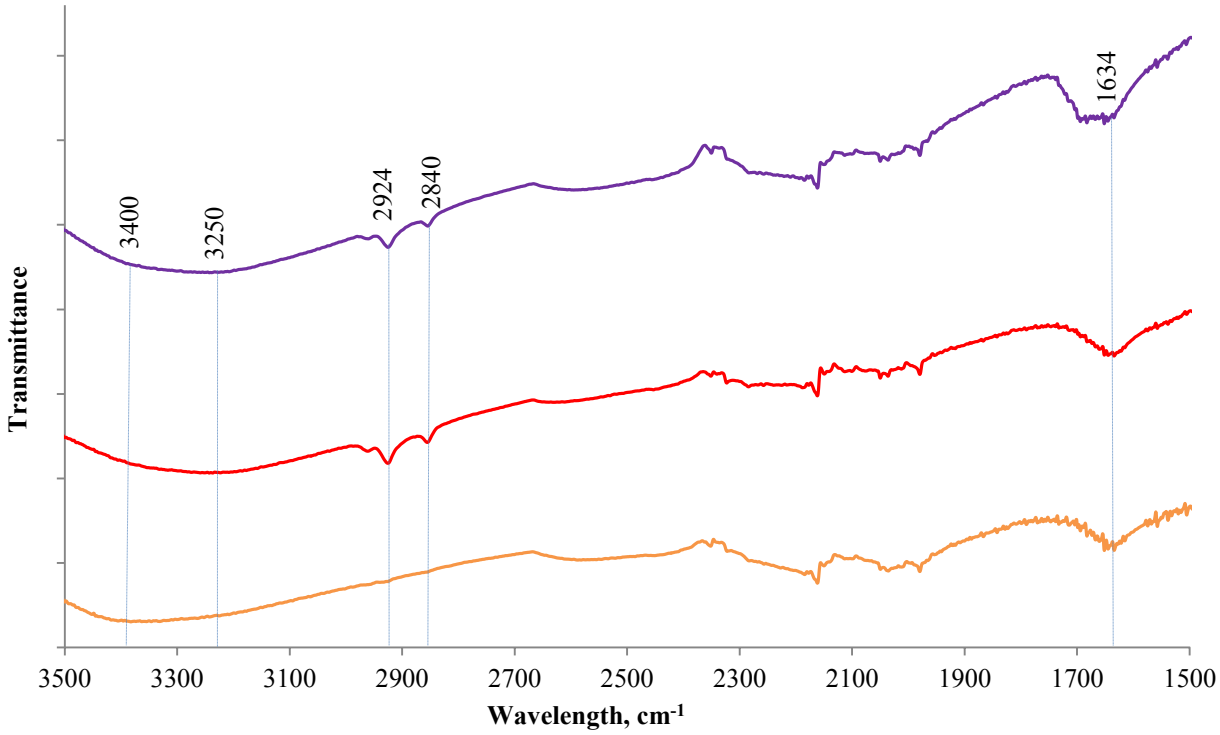


**Fig. 14.** FTIR spectra of $Fe_2O_3$-$TiO_2$ (purple), P25 (red), and $Fe_2O_3$ (brown).

**List of Tables**

**Table 1**

Comparison of catalyst characteristics among $Fe_2O_3$-$TiO_2$, P25 and $Fe_2O_3$.

| Sample | XRD | Surface analysis | | | Band gap energy, eV |
|---|---|---|---|---|---|
| | Crystallite size, nm | Specific surface area, $m^2/g$ | Pore volume, $cm^3/g$ | Pore size, nm | |
| $Fe_2O_3$-$TiO_2$* | 22.99 | 58.40 | 0.29 | 18.52 | 2.95 |
| P25 | 24.29 | 52.32 | 0.17 | 15.62 | 3.35 |
| $Fe_2O_3$ | 17.45 | 7.70 | 0.03 | 13.14 | 1.60 |

*Mechanochemical synthesis conditions: milling speed =250 rpm; [$Fe_2O_3$] =1 mol%; ball:powder mass ratio =10:1

**Table 2**

Textural properties of $Fe_2O_3$-$TiO_2$ at different milling time.

| Milling time, min | Surface analysis | | |
|---|---|---|---|
| | Specific surface area, $m^2/g$ | Pore volume, $cm^3/g$ | Pore size, nm |
| 10 | 55.57 | 0.26 | 16.16 |
| 15 | 56.99 | 0.28 | 17.22 |
| 20 | 58.40 | 0.29 | 18.52 |
| 25 | 55.18 | 0.24 | 15.29 |
| 30 | 52.41 | 0.22 | 15.00 |

Mechanochemical synthesis conditions: milling speed =250 rpm; [$Fe_2O_3$] =1 mol%; ball:powder mass ratio =10:1

**Table 3**

Crystallite properties of $Fe_2O_3$-$TiO_2$ at different milling speed.

| Milling speed, rpm | XRD analysis | |
|---|---|---|
| | Crystallite size, nm | Rutile phase fraction, % |
| 150 | 25.72 | 0.29 |
| 200 | 24.05 | 0.29 |
| 250 | 22.99 | 0.36 |
| 300 | 22.00 | 0.38 |
| 350 | 21.42 | 0.44 |

Mechanochemical synthesis conditions: milling time =20 min; [$Fe_2O_3$] =1 mol%; ball:powder mass ratio =10:1

**Table 4**

Control photocatalytic experiments.

| Control | COD removal, % |
|---|---|
| Photolysis | 0.1 |
| Catalysis (in the dark using $Fe_2O_3$-$TiO_2$) | 0.4 |
| P25 | 40.6 |
| Anatase $TiO_2$ | 24.9 |
| Rutile $TiO_2$ | 2.9 |
| $Fe_2O_3$ | 1.1 |